Research Article

Significantly improved corrosion resistance of Mg-15Gd-2Zn-0.39Zr alloys: Effect of heat-treatment

Jing Liu [a,1], Lixin Yang [b,1], Chunyan Zhang [b], Bo Zhang [b,*], Tao Zhang [c,*], Yang Li [c], Kaiming Wu [a], Fuhui Wang [c]

[a] *The State Key Laboratory of Refractories and Metallurgy, Hubei Province Key Laboratory of Systems Science in Metallurgical Process, International Research Institute for Steel Technology, Wuhan University of Science and Technology, 947 Heping Avenue, Wuhan, 430081, China*
[b] *Shenyang National Laboratory for Materials Science, Institute of Metal Research, Chinese Academy of Sciences, Shenyang, 110016, China*
[c] *Shenyang National Laboratory for Materials Science, Northeastern University, 3-11 Wenhua Road, Shenyang, 110819, China*

ABSTRACT

The effects of heat-treatment on corrosion behavior of Mg-15Gd-2Zn-0.39 Zr alloys were investigated through microstructure characterization, corrosion tests, and scanning Kelvin probe force microscope (SKPFM) analysis. In long-term corrosion experiments, the corrosion rates of Mg-Gd-Zn-Zr alloys were mainly determined by the effects of micro-galvanic corrosion. During heat-treatment, the β-$(Mg,Zn)_3Gd$ eutectic phase in as-cast alloys transformed into a long-period stacking ordered (LPSO) phase, coupled with the precipitation of small precipitates. As heat-treatment proceeded, the local potential and the volume fraction of the LPSO phases reduced gradually compared with the eutectic phase, which resulted in a remarkable decrease of the micro-galvanic effect between the second phase and Mg matrix. As a result, the corrosion resistance of heat-treated alloys improved significantly.

© 2019 Published by Elsevier Ltd on behalf of The editorial office of Journal of Materials Science & Technology.

1. Introduction

In recent years, Mg-RE (RE refers to rare earth elements) alloys have attracted much attention as one of the most promising structural materials due to their excellent comprehensive mechanical and creep resistance properties [1–12]. It can be concluded that, during heat-treatment, the high dispersion of long-period stacking ordered (LPSO) structure and the precipitation of transition phases provide the necessary strength and creep resistance to these alloys [10–16]. Table 1 presents some examples of the improved mechanical properties of Mg-RE alloys produced by heat-treatment [10,15–17]. However, the accompanying precipitation of the second phases during heat-treatment may promote the micro-galvanic corrosion of the adjacent Mg-matrix due to their noble nature [18–21]. It is well known that the low corrosion resistance has become one of the most important factors restricting the widespread application of Mg alloys [12,21–27]. Therefore, it

is crucial to explore the corrosion behavior of Mg-RE alloys after heat-treatment.

Unfortunately, most of the previous researches mainly focused on the effects of heat-treatment on mechanical properties of Mg-RE alloys, and ignored the corrosion behavior of these alloys. Only a few researchers investigated the effects of microstructure evolution during heat-treatment on corrosion behavior of Mg-RE alloys. Li et al. [28] analyzed the effects of microstructure evolution during T4 treatment on the corrosion resistance of Mg-Zn-Y alloys, and found that the dissolution of W phase in T4 treatment improved the corrosion property of T4 alloys. Yamasaki et al. [29,30] and Bi et al. [31] elucidated that both the cooling rate and cooling time affected the corrosion behavior of Mg-Zn-RE alloys by affecting the microstructure during cooling. In addition, Ma et al. [21] and Wang et al. [32] revealed that the corrosion resistance of Mg-Gd-Zn (Al) alloys was remarkably improved due to the precipitation of the LPSO phase during T6 heat-treatment. Zhang et al. [15,33] propounded that the biodegradation rates of Mg-Gd-Zn alloys in simulated body fluid were reduced after heat-treatment due to the profuse precipitation of LPSO phases. However, on the contrary, Bi et al. [31] and Zhao et al. [34] declared the detrimental effects of LPSO precipitation on the biodegradability of Mg-Zn-Y alloys and the corrosion resistance of Mg-Dy-Zn alloys respectively.

---

* Corresponding authors.
 E-mail addresses: bozhang@imr.ac.cn (B. Zhang), zhangtao@mail.neu.edu.cn (T. Zhang).
[1] These authors equally contributed to this work.

Table 1
Mechanical property of Mg-RE alloys under different heat-treatment conditions.

Alloy compositions (at.%)	Heat-treatment conditions	UTS (MPa)	YS (MPa)	Elongation	Ref.
Mg-1.7Gd-0.4Zn	As-cast	196	159	3.0	[17]
	T4 (773 K, 10 h)	299	181	5.3	
	T4+T6(498 K, peak-aged)	416	235	7.2	
	Extruded	335	191	9.0	
	Extruded + T6	384	203	5.6	
Mg-1Zn-2Gd	As-cast	162	150	63	[10]
	T4 (793 K, 2 h)	190	150	41	
	T4+T6 (473 K, 60 h)	240	190	67	
	T4+T6 (573 K, 10 h)	235	190	45	
Mg-9Gd-3Y-1Zn-0.8Mn	T4 (793 K, 10 h)	382	302	12.3	[16]
	T4+T6 (473 K, 1 h)	451	342	6.1	
Mg-9Gd-3Y-1Zn-0.8Mn-1.4Ag	T4 (793 K, 10 h)	433	350	10.6	[16]
	T4+T6 (473 K, 1 h)	533	399	9.0	
Mg-5Gd-1Zn-0.6Zr	T4 (793 K, 12 h)	220	110	15	[15]
	T4+ Extruded	265	214	31	
Mg-2.5Gd-1Zn-0.18 Zr	As-cast	220	139	4.2	Our research results
	T4 (773 K, 35 h)	236	129	10.6	
	T4+T6 (473 K, 128 h)	290	163	10.4	

To summarize, previous researches are only superficial descriptions about the effects of heat-treatment on the corrosion behavior and corrosion mechanism of Mg-RE alloys based on the results of immersion tests, hydrogen evolution experiments and electrochemical measurements. However, the intrinsic relationship between the corrosion behavior of Mg-RE alloys and their microstructural evolution during heat-treatment are scarce. Very few provide straightforward experiment data explaining the underlying corrosion mechanism. Therefore, the aim of the present study is to illustrate the effects of microstructure evolution during heat-treatment on the corrosion behavior of Mg-RE alloys by providing straightforward and quantitative experimental data. First, different types of Mg-15Gd-2Zn-0.39 Zr alloys were prepared under different heat-treatment conditions to present a comparative study. Then, the microstructure and corrosion behaviors of these alloys were characterized and measured. Further, the localized potential difference between the second phases and Mg matrix was measured by using a scanning Kelvin probe force microscope (SKPFM), and the effect of micro-galvanic was investigated quantitatively. Finally, the relationship between corrosion rate and microstructure evolution during heat-treatment was established.

2. Experimental procedures

2.1. Material preparation

The conventional ingot metallurgy process was employed to produce the as-cast Mg-15Gd-2Zn-0.39 Zr alloy (Mg-2.5Gd-1Zn-0.18 Zr at.%, denoted as Mg-Gd-Zn-Zr alloy for simplification). The composition of the studied Mg-Gd-Zn-Zr alloys was Gd-15, Zn-2.19, Zr-0.39, Al-0.0041, Si-0.0025, Fe-0.001, S-^{0}.0043, and Mg-balanced in wt%, which was analyzed using an inductive coupled plasma-atomic emission spectrometer (ICP-AES, X Series II).

The middle regions of the as-cast Mg-Gd-Zn-Zr alloys were cut into test coupons of 20 mm × 20 mm × 10 mm, and subsequently, the ingots were solid solution heat-treatment at 773 K for 35 h, followed by an immediate quenching in cold water (denoted as T4-treatment) [9]. Further, the T6 treatments were carried out at 473 K for 8 h, 128 h and 300 h, in order to obtain the under-aged, peak-aged and over-aged alloys, respectively [10,17] (denoted as T6-U, T6-P and T6-O alloys respectively). Before each experiment, the specimens were wet ground to a 2000 grit-finish by a SiC paper gradually. For SEM and SKPFM observations, the specimen surface was polished to a 0.5 μm-finish with ethanol lubricant. Afterwards, all the specimens were rinsed with distilled water and dried in a compressed hot air flow.

2.2. Microstructure characterization

An X-ray diffraction system (XRD, PHILIPS, PW1700) with Cu K_α radiation (λ = 1.5406 Å, 30 mA, 40 kV) was employed to identify the composition of Mg-Gd-Zn-Zr alloys, and the MDI Jade 5.0 software was used to analyze the obtained XRD patterns. A scanning electron microscope (SEM, PHILIPS, XL-30FG), equipped with an energy dispersive spectrometer (EDS) was used for micrograph observations. In order to reveal the microstructure of each phase in Mg-Gd-Zn-Zr alloys, a transmission electron microscope (TEM, JEOL, JEM-2100 F) and a high-resolution scanning transmission electron microscopy (HRSTEM, FEI, Tecnai-F30), equipped with a high-angle annular dark field (HAADF) detector and an energy dispersive spectrometer (EDS) were also utilized. TEM foils were prepared by argon ion milling. The spatial three-dimensional microstructure of the alloys were characterized by a high-resolution transmission X-ray tomography (HRTXT, X radia, VersaXRM-500). Moreover, the scanning Kelvin probe force microscope (SKPFM, Bruker Corporation, Multimode 3D) was employed to monitor the localized potential distribution in the studied alloys. The data acquisition process was carried out by two steps: first, the scanning probe height was set at 30 μm in order to obtain the relative height of surface morphology, and then, the probe scanned for the second time to acquire the potential information. The scan height was found to be 50 nm from the specimen surface according to the surface height in the first scan. The results of SKPFM were analyzed by NanoScope Analysis software.

2.3. Corrosion experiments

The 3.5 wt% NaCl solution saturated with Mg(OH)$_2$ (prepared by analytical grade reagents and deionized water) was used as the corrosion solution during the whole corrosion experiments. On one hand, the salt solution saturated with Mg(OH)$_2$ shows a stable pH value of around 10.3, ensuring the reproducibility of the electrochemical experiments. On the other hand, as Mg dissolves quickly, it is quite easy to obtain a high local pH value at its surface. Therefore, the Mg(OH)$_2$ saturated solution acts as a thin electrolyte layer adjacent to the My alloy surface in the NaCl solution to some extent. A constant test temperature of 30 ± 1 °C was maintained using a water bath throughout the corrosion experiments.

The corrosion rates of Mg-Gd-Zn-Zr alloy were evaluated by hydrogen evolution experiment, electrochemical impedance spectroscopy (EIS) measurement, and potentiodynamic polarization test. A set of self-developed apparatus including a beaker, a burette and a funnel was used for hydrogen evolution experiment [35].
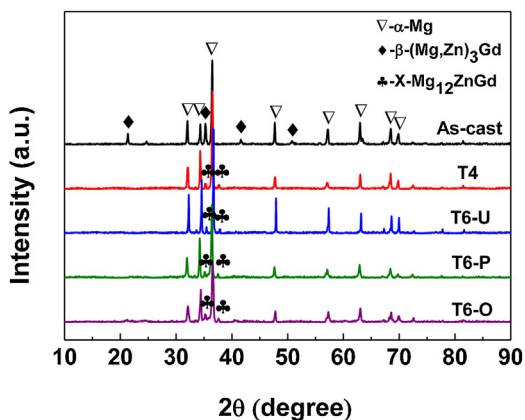
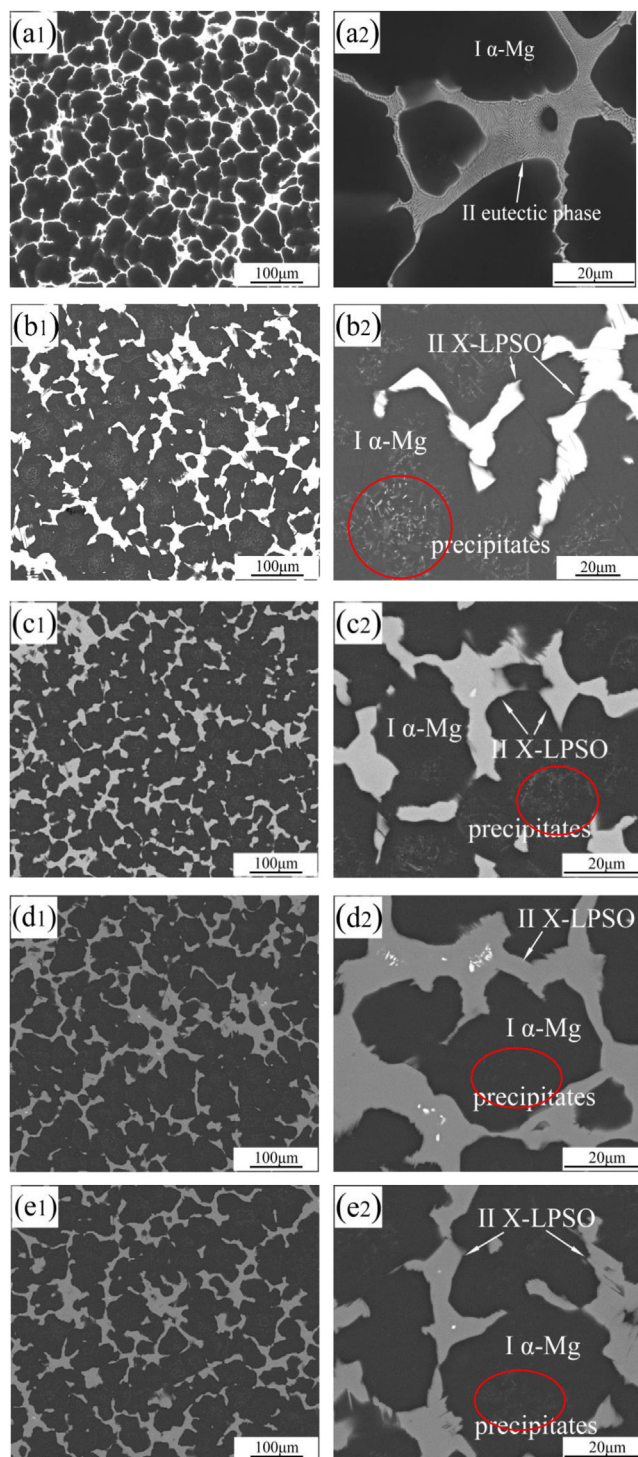**Fig. 1.** XRD patterns of Mg-Gd-Zn-Zr alloys under different heat-treatment conditions.

Fig. 2. SEM images of Mg-Gd-Zn-Zr alloys under different heat-treatment conditions: (a) as-cast, (b) T4, (c) T6-U, (d) T6-P, (e) T6-O.

When hydrogen bubbles were produced due to corrosion, a change was noticed in the solution height in the burette. Then the data were recorded continuously for 192 h for the calculation of the hydrogen evolution rate (HER). The electrochemical tests were carried out using a standard three-electrode cell in a Zahner Zennium electrochemical workstation, where a platinum plate was used as the counter electrode, a saturated calomel electrode (SCE) was employed as the reference electrode, and Mg alloy specimens acted as the working electrode. Before measurements, all the electrochemical specimens were embedded in epoxy resin leaving an exposed area of 4 cm^2 as the working electrode surface, and the other ends of the specimens were connected to a copper wire in order to create an electrical connection. EIS measurements were carried out over a frequency range from 100 kHz to 10 mHz by using a 5 mV amplitude sinusoidal voltage. The experimental data were analyzed by using the commercial software ZsimpWin. For polarization tests, the specimens were first stabilized at open circuit potential (OCP) for 30 min to reach a steady state. Then, the potentiodynamic scanning of cathode and anode was carried out separately at a uniform scan rate of 0.333 mV·s^{-1}. The polarization curve of the cathode ranged from OCP to -300 mV$_{vs.OCP}$, whereas, the potentiodynamic scan of the anode started from OCP untill the current density exceeded 5 mA·cm^{-2}. For better reproducibility, all the measurements of the corrosion rate were repeated at least three times.

The corrosion morphology observations were carried out by SEM. The specimens were immersed in the corrosion solution for 30 min at first. Afterwards, the corroded specimens were immersed in a chromate mixed solution (200 g/L CrO$_3$ + 10 g/L AgNO$_3$) for 1–3 min to remove the corrosion products. Then the specimens were washed with deionized water and dried by hot air flow. Meanwhile, the long-term corrosion morphologies were also observed. After immersed in the corrosion solution for 192 h, the specimens were directly washed with deionized water and dried by hot air flow for SEM observation.

3. Results

3.1. Microstructure characterization of Mg-Gd-Zn-Zr alloys

3.1.1. Microstructure evolution

Fig. 1 displays the XRD patterns of Mg-Gd-Zn-Zr alloys under different heat-treatment conditions. It was noticeable that the as-cast alloy was mainly consisted of α-Mg matrix and β-(Mg,Zn)$_3$Gd phase [13,16,36]. After T4 treatment, the eutectic phase disappeared, while a New X-Mg$_{12}$ZnGd phase transformed [22,32,37]. It

was worth mentioning that the compositions of T6 alloys remained the same with those of T4 alloys.

Fig. 2 and Table 2 present the SEM images and the EDS results of Mg-Gd-Zn-Zr alloys, respectively. The dark regions denote the α-Mg matrix and the light phases signify the second phases and the precipitates formed during heat-treatment. In Fig. 2(a), the dendrite-shape eutectic phases (the second phase was composed of β-(Mg,Zn)$_3$Gd with a lamellar microstructure) distributed continuously at the grain boundaries. The microstructure of T4 alloys was composed of an α-Mg solid solution, block-like X phases,

Table 2
EDS results of different regions in Fig. 2.

Alloys	Region	Mg	Gd	Zn	Zr
As-cast alloy	I	98.78	0.80	0.18	0.24
	II	87.60	7.70	4.70	0.00
T4 alloy	I	97.87	1.60	0.39	0.14
	II	91.27	5.11	3.62	0.00
T6-U alloy	I	97.96	1.46	0.34	0.24
	II	89.38	5.94	4.46	0.22
T6-P alloy	I	98.14	1.53	0.27	0.06
	II	90.19	5.72	4.00	0.09
T6-O alloy	I	97.97	1.56	0.32	0.15
	II	90.49	5.54	3.92	0.05
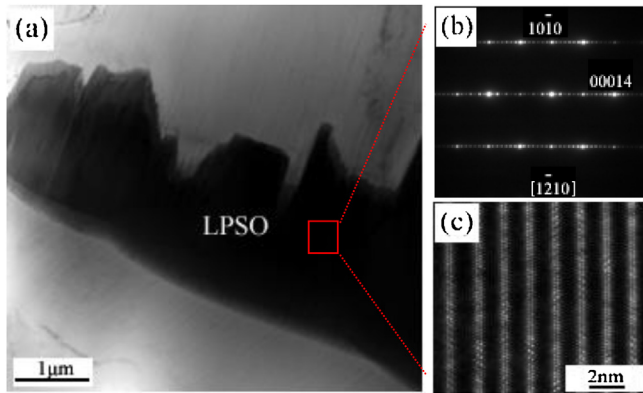
Fig. 3. (a) Bright-field TEM image of LPSO phase in T4 alloys. (b) SAED pattern of LPSO phase. Electron beam parallel to the $[1\bar{2}10]$ direction. (c) HRSTEM image of LPSO phase, indicating a 14H-LPSO structure.
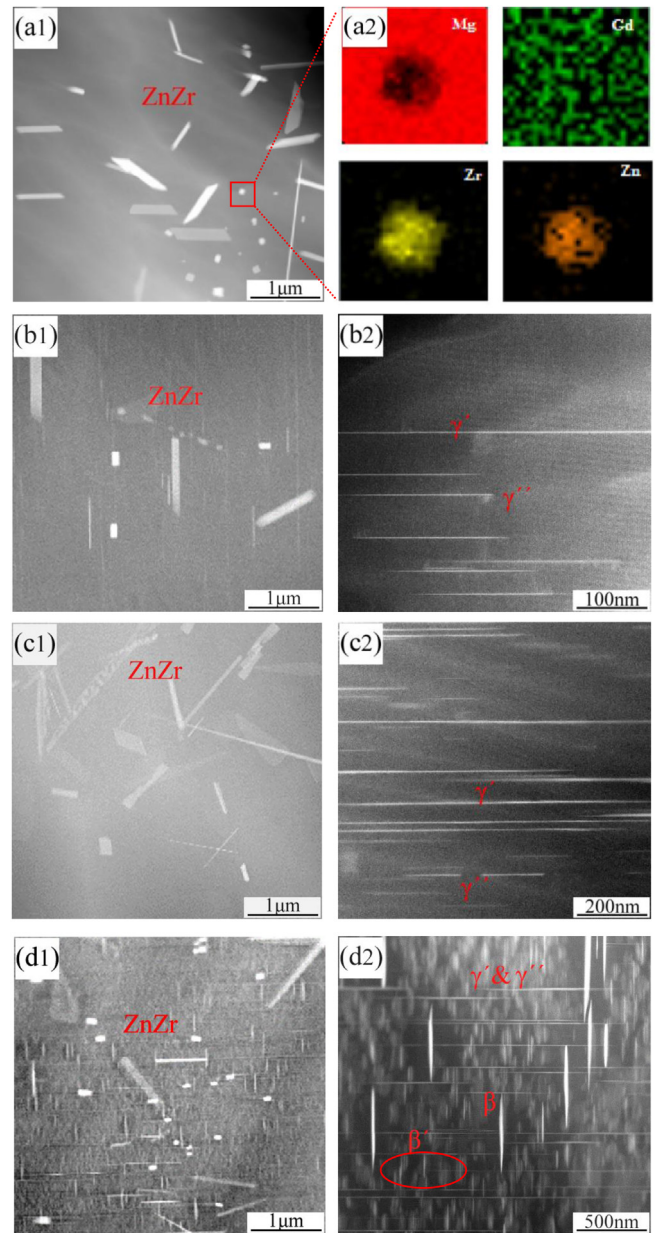

Fig. 4. HAADF-STEM images of precipitates in Mg-Gd-Zn-Zr alloys under different heat-treatment conditions: (a) T4, (b) T6-U, (c) T6-P, (d) T6-O. Especially, (a2) is the EDS mappings of a Zn-Zr particle by HRSTEM.

and a small number of precipitates distributed dispersively in the grains (Fig. 2(b)). Although the X phases were still distributed at the grain boundaries, they were not as consecutive as the eutectic phases. According to previous studies, the distribution and the block-shape of X phases revealed that they were obtained from the transition of eutectic phases. During T4-treatment, some of the alloying elements in the eutectic phases dissolved into Mg matrix, and the X phase with a 14H-type LPSO structure transformed when both the compositions and stacking orders were satisfied [11,32]. The LPSO phases were thermodynamic stable [9–11], and did not change during low-temperature aging treatment [10]. Therefore, after T6 treatment, the microstructure of LPSO phases in T6 alloys remained almost the same as those of T4 alloys (Fig. 2(c–e)). In order to further identify the microstructures of LPSO phases after T4 treatment, TEM and HRSTEM observations were made (Fig. 3). An obvious 14H-type LPSO structure was recognized from the selected area electron diffraction (SAED) patterns with the electron beam parallel to the $[1\bar{2}10]$ direction [9,22,37]. Moreover, the HRSTEM image in Fig. 3(c) further reveals the microstructure of LPSO phases. When the atoms lined up in horizontal direction in the graph, the atoms occurred periodically with a period of fourteen atoms, which proved the 14H-LPSO structure.

However, the precipitates formed during heat-treatment were too small and scarce to be identified by XRD and EDS analysis. The microstructures of the precipitates were further analyzed by HAADF-STEM technique (Fig. 4). The small rod-like precipitates in T4 alloys were identified as Zn-Zr particles by EDS mappings. During T6 treatment, a new γ''-$Mg_{70}Gd_{15}Zn_{15}$ phase with needle-like shape was formed in T6-U alloys [8]. With the prolonged aging time, the T6-P alloys yielded a γ'-MgGdZn phase after the precipitation of Zn-Zr particles and γ'' phases [8]. The γ' phase was similar to γ'' phase but with a longer length in morphology. Zn-Zr particles, γ'' and γ' phases were all thermodynamically stable to 300 h of

aging. The T6-O alloys precipitated spindle-like β' and β phases with a composition of Mg_5Gd [10,17], which were perpendicular to γ'' and γ' phases. It was found that the total number of precipitates increased after T6 treatment. However, it was still low as compared to the second phases exhibited in the SEM images (Fig. 2).

3.1.2. Three-dimensional distribution

In order to obtain a comprehensive understanding of the microstructures of different phases of Mg-Gd-Zn-Zr alloys, HRTXT was applied to characterize the three-dimensional distribution of each phase and also to calculate their volume fraction statistically. It could be seen in Fig. 5 that, the eutectic phases in as-cast alloys exhibited a honeycomb-like network in the three-dimensional mapping, with a high volume fraction of 42.8%. In contrast, LPSO phases manifested a discontinuous block-like shape with varying volume fractions of 20%–27% in different alloys. With regards to the small precipitates, only Zn-Zr particles could be examined by
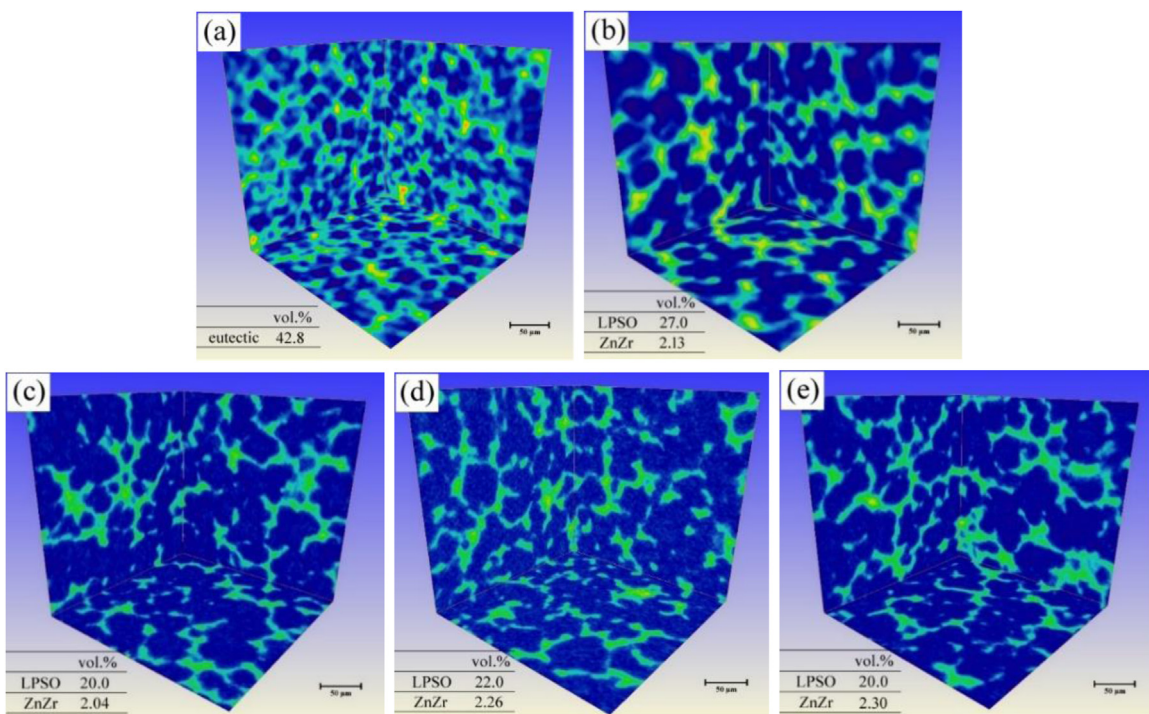
Fig. 5. Three-dimensional distribution images of (a) as-cast, (b) T4, (c) T6-U, (d) T6-P, and (e) T6-O alloys by HRTXT.

HRTXT, whose volume fractions merely occupied 2.0%–2.3% according to the statistical results of the apparatus. However, the volume fractions of other precipitates couldn't be calculated by HRTXT due to their lower volume fractions or smaller sizes as compared to Zn-Zr particles.

3.2. Corrosion rate of Mg-Gd-Zn-Zr alloys

3.2.1. Hydrogen evolution experiments

With respect to the determination of the corrosion rates of Mg alloys, the most accurate and precise method is probably the hydrogen evolution experiment for long-time corrosion tests [38–40]. Therefore, the hydrogen evolution volume of Mg-Gd-Zn-Zr alloys under different heat-treatment conditions was recorded continuously for 192 h and the HER was calculated according to Eq. (1) below.

$$HER = \frac{\Delta V}{S \Delta t} \tag{1}$$

where ΔV represents the hydrogen evolution volume at a certain time interval (mL), S is the specimen's area (cm^2), and Δt is the time interval (h).

Fig. 6 displays the HER results. The variation tendency of HER can be divided into three stages. First, in the initial 24 h (stage I), the HER of as-cast alloys yielded a low level, whereas, it increased continuously for heat-treated alloys. As a results, the HER values of T4 and T6 alloys were slightly higher than that of as-cast alloys. Afterwards, in the time interval of 24 h–72 h (stage II), the HER of as-cast alloys increased rapidly due to some reasons (which would be discussed later); However, heat-treated alloys presented a moderate tendency in the variation of HER. Finally, in the following immersion tests (stage III), the HER of as-cast alloys reached to a high level of about 1.02 mL·cm^{-2} h^{-1} and presented a steady state in the end of the experiment. With respect to heat-treated alloys, the corrosion rate didn't change anymore except for a little decrease of HER. The final HER values of heat-treated alloys were 0.12 (T4), 0.14 (T6-U), 0.14 (T6-P), and 0.08 (T6-O) mL·cm^{-2} h^{-1}, respectively. The

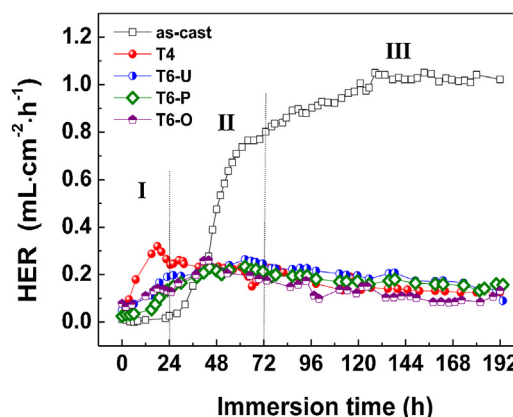**Fig. 6.** Hydrogen evolution rate (HER) of Mg-Gd-Zn-Zr alloys at different immersion time.

HER reduced in the following order: as-cast»T4≈T6-U≈T6-P > T6-O alloys, indicating that heat-treatment process was beneficial to improve the corrosion resistance significantly during long time corrosion tests.

3.2.2. EIS measurements

EIS measurements were carried out for as-cast and heat-treated alloys during the long-time immersion. The EIS results at typical immersion periods (that is, 0 h, 24 h, 72 h, and 192 h according to the results of hydrogen evolution experiments) are depicted in Fig. 7. The impedance spectrum of the as-cast alloys at the beginning of the immersion was consisted of a capacitive loop in the high frequency range, a capacitive loop in the middle frequency range and an inductive loop in the low frequency range. Nevertheless, all of the heat-treated alloys and as-cast alloys immersed for a period exhibited a capacitive loop in the high frequency range and an inductive loop in the low frequency range.
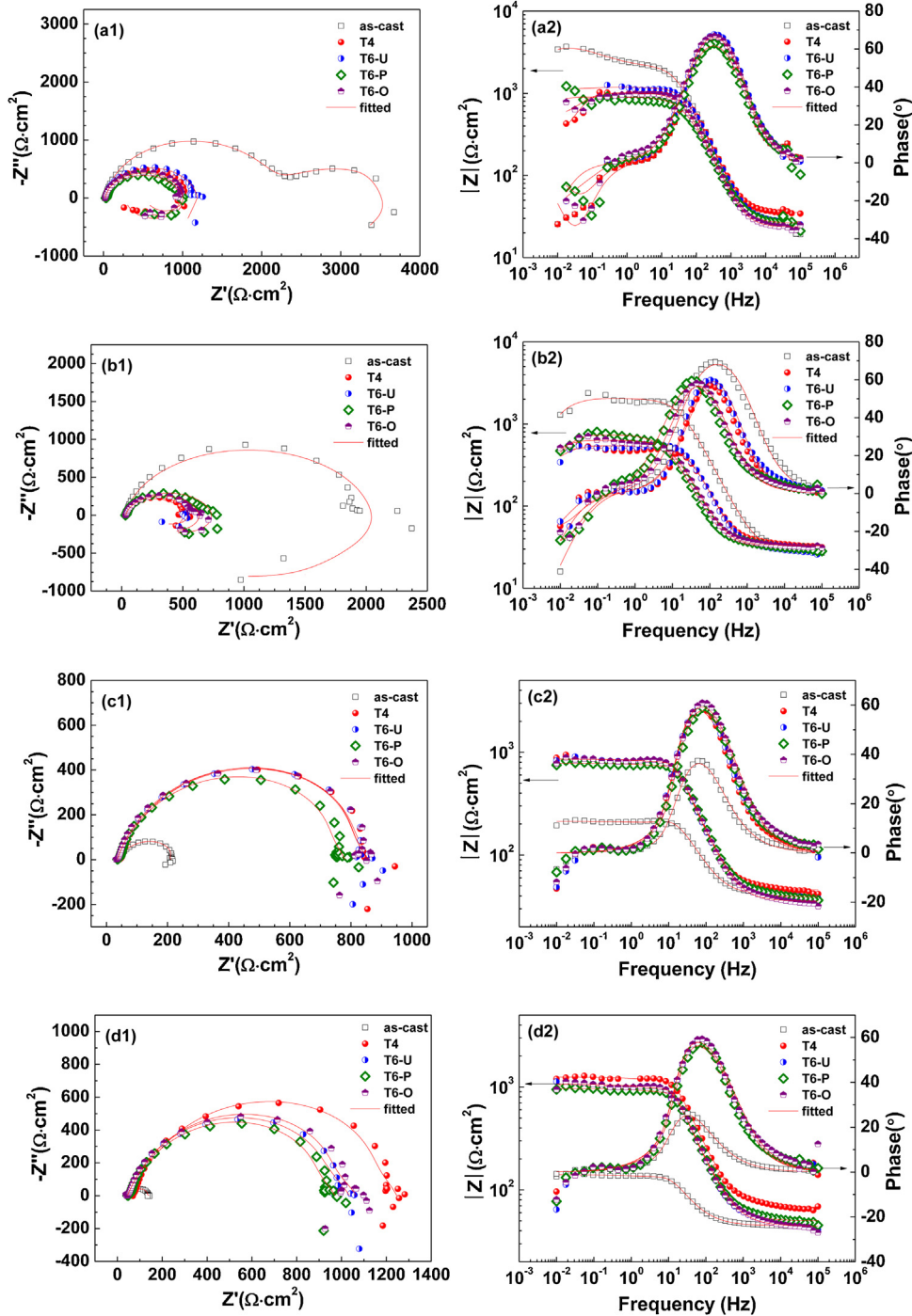
Fig. 7. EIS of Mg-Gd-Zn-Zr alloys after immersion for (a) 0 h, (b) 24 h, (c) 72 h, and (d) 192 h. (a1-d1) are Nyquist plots and (a2-d2) are Bode plots.

The equivalent circuits in Fig. 8 are used for fitting the EIS data, where R_s is the solution resistance; CPE_f and R_f represent the constant phase element of corrosion product and its film resistance; CPE_{dl} is the double layer capacitance and R_{ct} is the charge transfer resistance; L is the inductance which represents the breakdown of the partial protective film on alloys surface and R_L is the resistance of inductance [41–45]. It can be inferred that the corrosion process of heat-treated alloys and as-cast alloys immersed for a period might be the same; whereas, the double capacitive loop of as-cast alloys in the initial stage should be a reflection of the protectiveness of product film.

The polarization resistance, R_p, is an important parameter for the evaluation of the corrosion resistance, the reciprocal of which is proportional to the corrosion rate. According to the fitting results of the equivalent circuits, R_p can be calculated as follows:

$$R_p = R_s + R_f + \frac{R_{ct} \cdot R_L}{R_{ct} + R_L} \tag{2}$$

(Fig. 8(a))

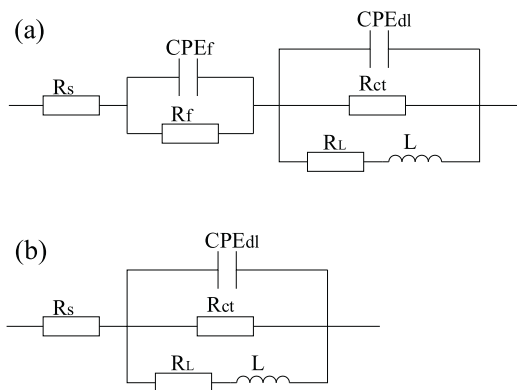$$R_p = R_s + \frac{R_{ct} \cdot R_L}{R_{ct} + R_L} \tag{3}$$

(Fig. 8(b))

Fig. 8. Equivalent circuits for (a) as-cast alloys at the beginning of the immersion, and (b) as-cast alloys immersed for a period and heat-treated alloys.
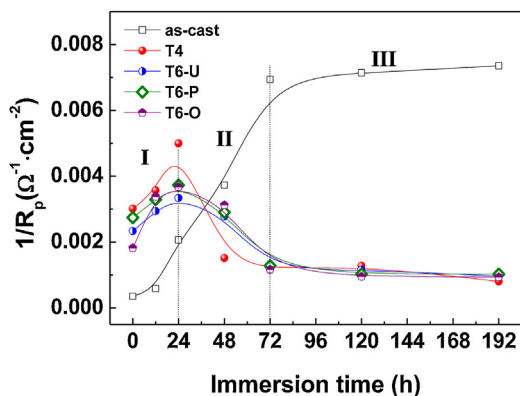

Fig. 9. $1/R_p$ of Mg-Gd-Zn-Zr alloys during various immersion time obtained from EIS.

Fig. 10. Potentiodynamic polarization curves of Mg-Gd-Zn-Zr alloys under different heat-treatment conditions.

Therefore, $1/R_p$ was calculated and shown in Fig. 9. In general, the variation of $1/R_p$ was in great consistent with hydrogen evolution results. In the long-term immersion test, heat-treated alloys exhibited lower values of $1/R_p$ than that of as-cast alloys, demonstrating a better corrosion resistance of heat-treated alloys than as-cast alloys further.

3.2.3. Potentiodynamic polarization tests

The potentiodynamic polarization curves of Mg-Gd-Zn-Zr alloys under different heat-treatment conditions are shown in Fig. 10. It showed that the anodic polarization behavior of the as-cast alloys was distinctly different from those of the heat-treated alloys. The as-cast alloys presented an obvious self-passive characteristic, while the heat-treated alloys presented a similar active dissolution for both T4 and T6 alloys. The self-passivation of the as-cast alloys was just a manifestation for the existence of the product film at the initial immersion period, as exhibited in the double capacitance loops in EIS (Fig. 7(a)). The polarization curves were fitted and the results are shown in Table 3. There was a lower corrosion current density (i_{corr}) for the as-cast alloy than the heat-treated alloys, which was agree with the corrosion rate of hydrogen evolution experiments and EIS measurements in the initial stage. It should be mentioned that the corrosion potential (E_{corr}) of the as-cast alloy was lower than the heat-treated alloys, which could be
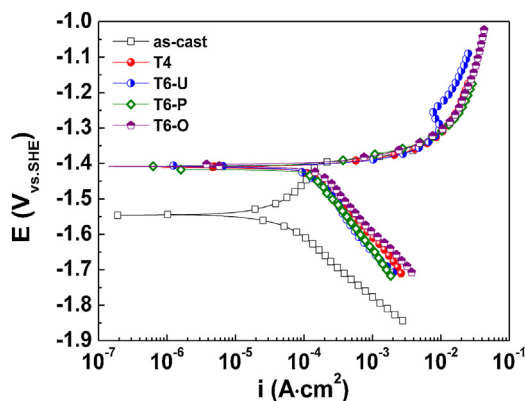
explained by the mixed potential theory. As the deposition of product film, the cathodic hydrogen evolution process was restrained, and as a result, the intersection of anode and cathode shifted to a lower potential.

3.3. Corrosion morphology

After immersion in the corrosion solution for 30 min, the initial corrosion morphologies of the as-cast alloys and heat-treated alloys are exhibited in Fig. 11. The contrast of the extent of corrosion was obvious. Heat-treated alloys presented a more severe corrosion morphologies than as-cast alloys, which demonstrated a lower corrosion rate for as-cast alloys in the initial stage, as illustrated in the results of corrosion rate. For better observation of the corrosion initiation sites, a prolonged immersion was implemented for as-cast alloys. Further observation revealed that all of the studied alloys presented a typical micro-galvanic corrosion feature. There were lots of corrosion pores occurred in the α-Mg matrix uniformly, while, the second phase presented incorrosive state. That is to say, the α-Mg matrix was the preferential corroded phase, and the second phases, acting as cathodic phases, promoted the dissolution of the adjacent Mg matrix.

During a long-term immersion, there was a deposition of corrosion product layer, which was composed of a loose and laminated inner layer, and a compact outer layer, as seen the cross-section micrographs in Fig. 12. The corrosion product layer of the as-cast alloys was thicker than those of the heat-treated alloys, indicating a faster corrosion rate of as-cast alloys in the long-term corrosion test. Meanwhile, several residual second phases were found in the corrosion product layer, which could be ascribed to the fall off of the second phases after the dissolution of the surrounding Mg matrix, implying that the micro-galvanic corrosion was still the main corrosion process throughout the whole experiments.

3.4. Local potential distribution

SKPFM is a powerful tool for the investigation of micro-electrochemical behavior in corrosion research. Therefore, in present experiments, the local potential distributions of Mg-Gd-Zn-Zr alloys under different heat-treatment conditions were monitored by SKPFM. According to the results of SKPFM mapping

Table 3
Electrochemical parameters obtained from potentiodynamic polarization curves in Fig. 10.

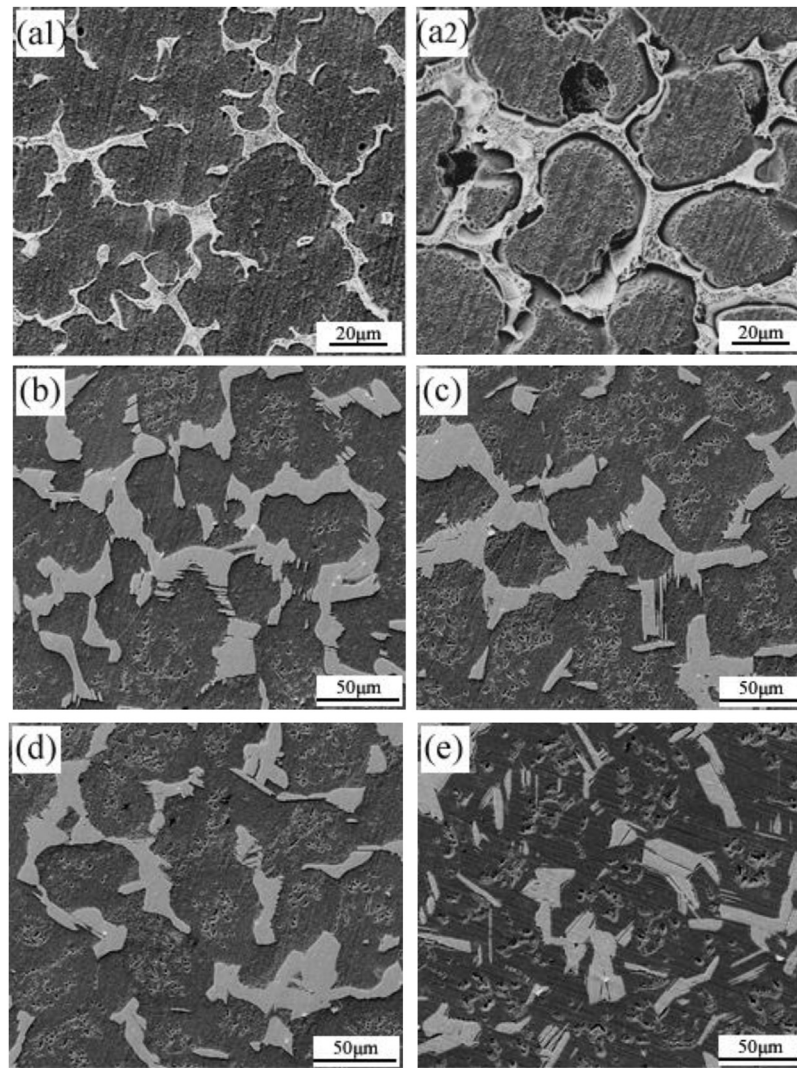|	As-cast	T4	T6-U	T6-P	T6-O
E_{corr} (V)	−1.54	−1.41	−1.41	−1.41	−1.41
i_{corr} (A·cm^{-2})	0.43×10^{-4}	1.16×10^{-4}	0.95×10^{-4}	1.23×10^{-4}	1.39×10^{-4}

Fig. 11. SEM images of the initial corrosion morphologies of (a1) as-cast, (b) T4, (c) T6-U, (d) T6-P and (e) T6-O alloys after immersed in corrosion solution for 30 min. (a2) is the corrosion morphology of as-cast alloys immersed for 1 h.

and line-profile analysis displayed in Fig. 13, the local potential differences between the second phases (eutectic phase or LPSO phase) and α-Mg matrix are 290 mV, 243 mV, 236 mV, 207 mV and 170 mV for as-cast, T4, T6-U, T6-P and T6-O alloys, respectively. It revealed that the relative potentials of the second phases decreased gradually as heat-treatment proceeded, indicating a substantial reduced acceleration effect of the second phase in micro-galvanic corrosion. Comparing with the value of $1/R_p$, it is easy to find that the local potential is positively correlated with the corrosion rate. The higher the local potential difference, the higher the tendency of the micro-galvanic corrosion, and therefore, the higher the value of $1/R_p$. SKPFM results not only provide a theoretical explanation for the micro-galvanic corrosion phenomenon that observed in Fig. 11, but also provide a quantitative description for the degree of micro-galvanic corrosion.

4. Discussion

SEM images (Fig. 11) and SKPFM results (Fig. 13) have illustrated that the micro-galvanic corrosion is the main corrosion mechanism for the studied Mg-RE alloys. Therefore, the corrosion behavior of these alloys is mainly affected by the effect of the second phases.

Meanwhile, the compact outer layer of the corrosion product also has an effect on the corrosion behavior.

For as-cast Mg-Gd-Zn-Zr alloys, the HER was small in the initial stage (stage I). Due to the deposition of $Mg(OH)_2$ in the test solution, the product film acting as a barrier hindered the penetration of corrosive ion and further corrosion process [46], and therefore led to a lower HER. The double capacitive loops in EIS and the passive region in anodic polarization curve were the best evidences for the protectiveness of the product film. After a period of pregnant and propagation of corrosion, the micro-galvanic corrosion between eutectic phase and Mg matrix broke up the passivity of the product film. There was no double capacitive loop in EIS anymore. As a result, the eutectic phases acting as a cathode would evoke a severe micro-galvanic corrosion according to the SKPFM results. The high relative potential (290 mV) of eutectic phase accelerated the corrosion of the adjacent α-Mg matrix during micro-galvanic corrosion. As illustrated in Fig. 9, the decrease of R_p was a reflection of the increase of the mass-transfer process, which indicated the increase of the micro-galvanic corrosion rate. Therefore, a rapid increase of HER in the subsequent immersion test (stage II) occurred. Finally, under the acceleration effect of the micro-galvanic corrosion and the barrier effect of the corrosion product layer, the corrosion of as-cast alloys reached to a
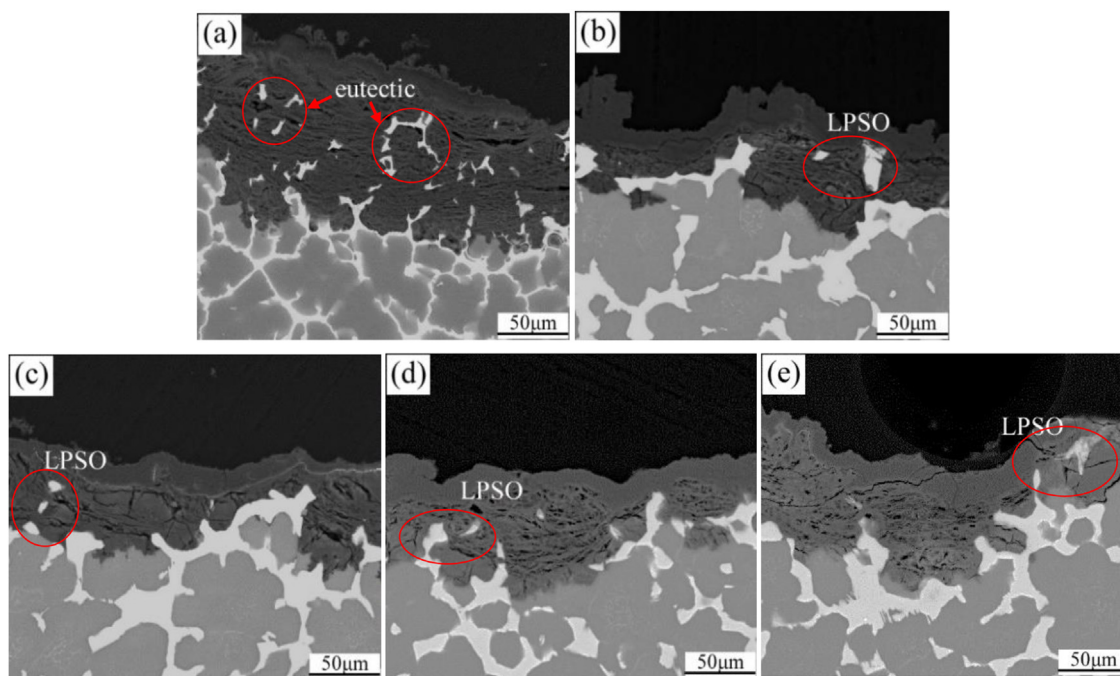
Fig. 12. SEM images of the cross-section corrosion morphologies of (a) as-cast, (b) T4, (c) T6-U, (d) T6-P, and (e) T6-O alloys after immersed in corrosion solution for 192 h.

steady state and presented a HER value of about 1.02 mL·cm^{-2} h^{-1} (stage III).

However, the situation was entirely different for heat-treated alloys in the initial stage (stage I). The EIS results manifested that there was no protection effect of the product film for heat-treated alloys. The Zn-Zr particles in heat-treated alloys induced a drastic micro-galvanic corrosion in the initial stage due to their noble nature (the relative potential was as high as 426 mV, which was reported in our other research), which broke up the protectiveness of the product film of Mg(OH)$_2$. Therefore, the HER was relative higher than as-cast alloys. Combined with the SKPFM results, the LPSO phases also promoted the micro-galvanic corrosion of the matrix due to their high local potentials. As a result, the HER increased gradually for heat-treated alloys in the initial stage. In the subsequent long-term corrosion test (stage II and III), the influencing factors of the corrosion behavior didn't change. It was still the acceleration effect of the second phases in micro-galvanic corrosion that promoted the corrosion of Mg matrix. With the benefit of the deposition of the compact corrosion product layer, the variation of HER presented a moderate tendency except for a little decrease in the end of the experiments. Correspondingly, the loops in EIS remained the same and the values of $1/R_p$ decreased gradually after a period of steady change.

It should be mentioned that there was a big difference of HER between as-cast alloys and heat-treated alloys in the long-term corrosion test. The EIS of both as-cast and heat-treated alloys exhibited a similar capacitive and inductive loops, while the values of $1/R_p$ appeared big difference, which manifested that the difference of HER should be ascribed to the difference of the micro-galvanic effect. The micro-galvanic effect is determined by two factors: one is the local potential difference, the other is the volume fraction, which are displayed in Table 4 provided by SKPFM and HRTXT results. For as-cast alloys, the local potential difference between eutectic phase and Mg matrix was 290 mV. When combined with the high volume fraction of the eutectic phase, the effect of micro-galvanic corrosion was obvious, leading to a high HER. After T4 treatment, some of the alloying elements in eutectic phases dissolved into the Mg matrix, and a new LPSO phase transformed. Due

to the difference of chemical compositions, the local potential of LPSO phases reduced to 243 mV relative to Mg matrix. Meanwhile, the volume fractions of the second phases decreased from 42.8% to 27%. Therefore, the effect of micro-galvanic corrosion reduced significantly for T4 alloys as compared to as-cast alloys, resulting in an absolutely low HER. During T6 treatment, the compositions and the volume fractions of LPSO phases did not change too much. However, the dispersive distribution of the precipitates such as γ″, γ′, β′ and β phases during T6 treatment improved the absolute potential of the α-Mg matrix due to their noble nature [18,21]. Therefore, the relative potentials between LPSO phases and α-Mg matrix reduced, which varied from 236 mV to 170 mV for T6 alloys as aging time prolongs. Moreover, the volume fraction of the LPSO phases decreased a little, from 27% to 20%–22%. Therefore, the effect of micro-galvanic corrosion reduced further for T6 alloys. Consequently, T6-O alloys yielded the lowest HER. It was worth mentioning that the micro-galvanic effects between small precipitates (Zn-Zr particles, γ″, γ′, β′ and β phases) and the α-Mg matrix were ignored, because these precipitates were too small (in both size and volume fraction) to perform an effective micro-galvanic corrosion.

The correlation between microstructure characteristic and corrosion rate are illustrated in Fig. 14. To summarize, heat-treatment brought about remarkable evolution of the microstructure, which reduced the micro-galvanic effect between the second phases and Mg matrix, and therefore, resulted in a significantly improved corrosion resistance of Mg-Gd-Zn-Zr alloys.

5. Conclusion

During the long-term corrosion experiments, the corrosion rates of Mg-Gd-Zn-Zr alloys were mainly determined by the effects of micro-galvanic corrosion. According to SKPFM and HRTXT results, the eutectic phase in as-cast alloys possessed the highest local potential difference (290 mV) and volume fraction (42.8%), and therefore, there was a remarkable micro-galvanic effect between eutectic phase and Mg matrix. As a result, the corrosion rate of as-cast alloys was high (1.02 mL·cm^{-2} h^{-1}). However, after T4 treatment, the eutectic phase in as-cast alloys transformed into a LPSO
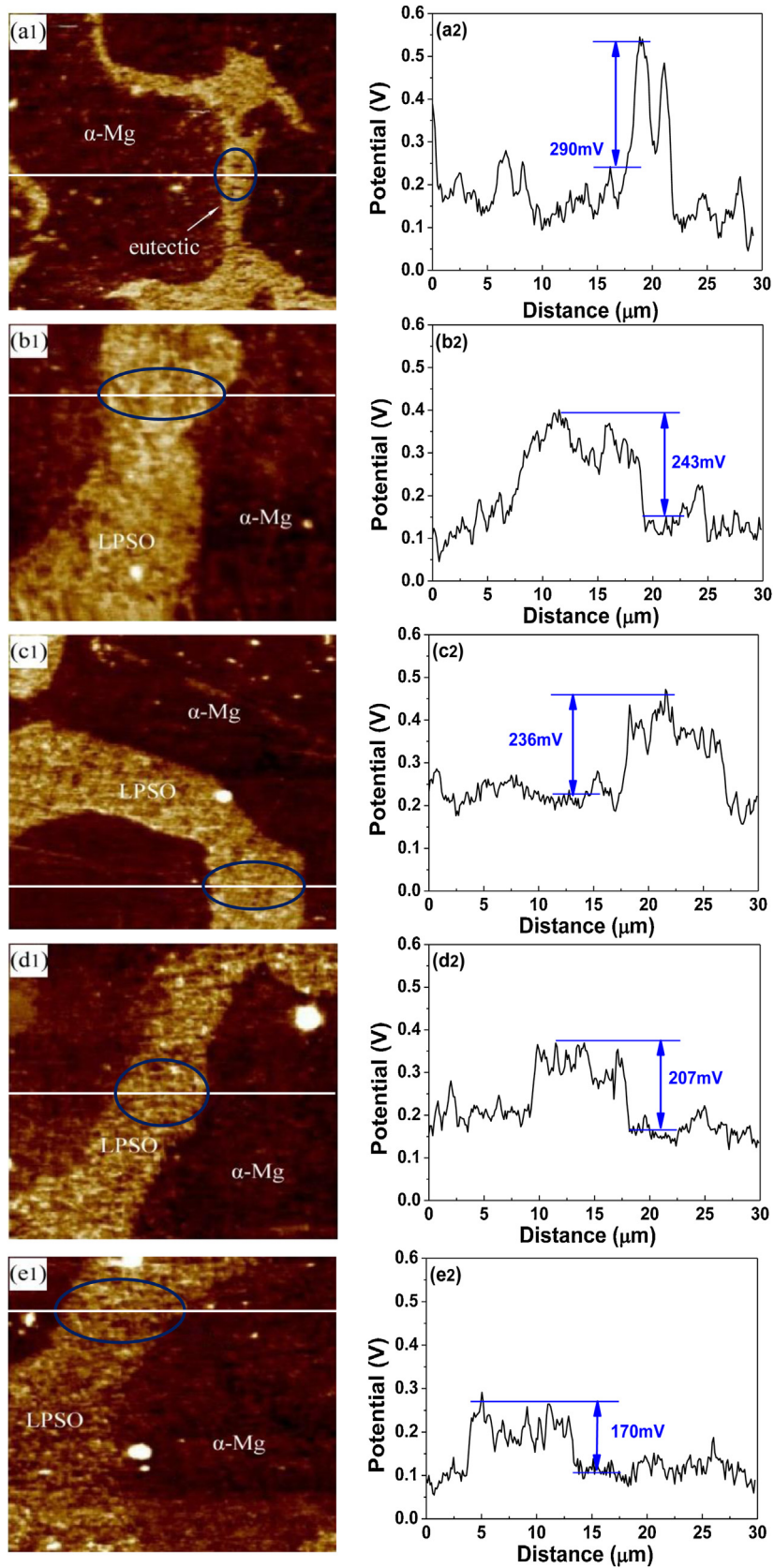
Fig. 13. SKPFM results of the local potential distribution between second phases and α-Mg matrix in (a) as-cast, (b) T4, (c) T6-U, (d) T6-P and (e) T6-O alloys.

Table 4
Parameters related to the microstructure characteristic and corrosion rate of Mg-Gd-Zn-Zr alloys.

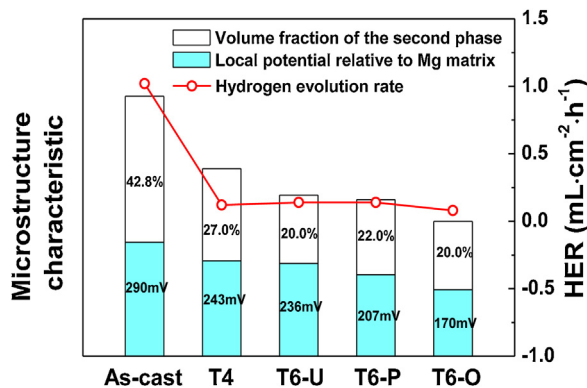| Alloys	Second phases		Potential relative to matrix (mV)	Volume fraction (%)		HER of 192 h (mL·cm^{-2}·h^{-1})
As-cast	β-(Mg,Zn)$_3$Gd eutectic phase		290	42.8		1.02
T4 alloy	LPSO		243	27.0		0.12
	ZnZr		426	2.13		
T6-U alloy	LPSO		236	20.0		0.14
	ZnZr	γ"	426	/	2.04 /	
T6-P alloy	LPSO		207	22.0		0.14
	ZnZr	γ"+γ'	426	/	2.26 /	
T6-O alloy	LPSO		170	20.0		0.08
	ZnZr	γ"+γ'+β'+β	426	/	2.30 /	

Fig. 14. Schematic diagram of the relationship between the microstructure characteristic and corrosion rate of Mg-Gd-Zn-Zr alloys.

phase. The local potential and the volume fraction of LPSO phases reduced compared to eutectic phases, which were 243 mV and 27% respectively. Therefore, the micro-galvanic effect between the second phase and Mg matrix reduced a lot, resulting in a significantly decreased HER value of 0.12 mL·cm^{-2} h^{-1}. Afterwards, the microstructure and compositions of LPSO phases did not change during T6 treatment. But the dispersive distributed precipitates improved the potential of α-Mg matrix slightly. Hence, the corrosion resistance of Mg-Gd-Zn-Zr alloys was improved again due to a further reduction in the micro-galvanic effect. The T6-O alloys yielded the lowest corrosion rate of about 0.08 mL·cm^{-2} h^{-1}.

Acknowledgements

References

[1] H. Liu, J. Bai, K. Yan, J.L. Yan, A.B. Ma, J.H. Jiang, Mater. Des. 93 (2016) 9–18.
[2] W.T. Sun, X.G. Qiao, M.Y. Zheng, C. Xu, S. Kamado, X.J. Zhao, H.W. Chen, N. Gao, M.J. Starink, Acta Mater. 151 (2018) 260–270.
[3] J.W. Chang, X.W. Guo, P.H. Fu, L.M. Peng, W.J. Ding, Electrochim. Acta 52 (2007) 3160–3167.
[4] X.W. Guo, J.W. Chang, S.M. He, W.J. Ding, X.S. Wang, Electrochim. Acta 52 (2007) 2570–2579.
[5] L. Xiao, G.Y. Yang, Y. Liu, S.F. Luo, W.Q. Jie, J. Mater. Sci. Technnol. 34 (2018) 2246–2255.
[6] J.Y. Han, J. Chen, L.M. Peng, S. Tan, Y.J. Wu, F.Y. Zheng, H. Yi, Mater. Des. 130 (2017) 90–102.
[7] I. Stulikova, B. Smola, J. Cizek, T. Kekule, O. Melikhova, H. Kudrnova, J. Alloys. Compd. 738 (2018) 173–181.
[8] J.F. Nie, K. Oh-ish, X. Gao, K. Hono, Acta Mater. 56 (2008) 6061–6076.
[9] Y.J. Wu, X.Q. Zeng, D.L. Lin, L.M. Peng, W.J. Ding, J. Alloys. Compd. 477 (2009) 193–197.
[10] M. Yamasaki, M. Sasaki, M. Nishijima, K. Hiraga, Y. Kawamura, Acta Mater. 55 (2007) 6798–6805.
[11] D.J. Li, X.Q. Zeng, J. Dong, C.Q. Zhai, W.J. Ding, J. Alloys. Compd. 468 (2009) 164–169.
[12] G.L. Bi, Y.D. Li, S.J. Zang, J.B. Zhang, Y. Ma, Y. Hao, J. Magnes. Alloys 2 (2014) 64–71.
[13] D.K. Xu, E.H. Han, Y.B. Xu, Progr. Nat. Sci.: Mater. Int. 26 (2016) 117–128.
[14] C.Q. Li, D.K. Xu, Z.R. Zeng, B.J. Wang, L.Y. Sheng, X.B. Chen, E.H. Han, Mater. Des. 121 (2017) 430–441.
[15] X.B. Zhang, Z.X. Ba, Z.Z. Wang, Y.J. Wu, Y.J. Xue, Mater. Lett. 163 (2016) 250–253.
[16] J.F. Wang, K. Wang, F. Hou, S.J. Liu, X. Peng, J.X. Wang, F.S. Pan, Mater. Sci. Eng. A 728 (2018) 10–19.
[17] R. Zhen, Y.S. Sun, F. Xue, J.J. Sun, J. Bai, J. Alloys. Compd. 550 (2013) 273–278.
[18] S. Cabeza, G. Garceś, P. Peŕez, P. Adeva, J. Mech. Behav. Biomed. Mater. 46 (2015) 115–126.
[19] N. Birbilis, M.K. Cavanaugh, A.D. Sudholz, S.M. Zhu, M.A. Easton, M.A. Gibson, Corros. Sci. 53 (2011) 168–176.
[20] G.L. Song, A. Atrens, Adv. Eng. Mater. 5 (2003) 837–858.
[21] F.M. Lu, A.B. Ma, J.H. Jiang, Y. Guo, D.H. Yang, D. Song, J.Q. Chen, Corros. Sci. 94 (2015) 171–178.
[22] A. Srinivasan, Y. Huang, C.L. Mendis, C. Blawert, K.U. Kainer, N. Hort, Mater. Sci. Eng. A 595 (2014) 224–234.
[23] C.Q. Li, D.K. Xu, Z.R. Zeng, B.J. Wang, L.Y. Sheng, X.B. Chen, E.H. Han, Mater. Des. 121 (2017) 430–441.
[24] J.S. Zhang, J.D. Xu, W.L. Cheng, C.J. Chen, J.J. Kang, J. Mater. Sci. Technol. 28 (2012) 1157–1162.
[25] F. Shi, C.Q. Wang, Z.M. Zhang, Trans. Nonferrous Met. Soc. China 25 (2015) 2172–2180.
[26] X.W. Yu, B. Jiang, J.J. He, B. Liu, F.S. Pan, J. Alloys. Compd. 749 (2018) 1054–1062.
[27] Y.W. Song, D.Y. Shan, E.H. Han, J. Mater. Sci. Technol. 33 (2017) 954–960.
[28] Z.M. Li, D.Q. Wan, Y. Huang, S.T. Ye, Y.L. Hu, J. Magnes. Alloys 5 (2017) 217–224.
[29] S. Izumi, M. Yamasaki, Y. Kawamura, Corros. Sci. 51 (2009) 395–402.
[30] M. Yamasaki, S. Izumi, Y. Kawamura, H. Habazaki, Appl. Surf. Sci. 257 (2011) 8258–8267.
[31] G.L. Bi, J. Jiang, F. Zhang, D.Q. Fang, Y.D. Li, Y. Ma, Y. Hao, J. Rare Earths. 34 (2016) 931–937.
[32] J.F. Wang, W.Y. Jiang, Y. Ma, Y. Li, S. Huang, Mater. Chem. Phys. 203 (2018) 352–361.
[33] X.B. Zhang, Q. Wang, F.B. Chen, Y.J. Wu, Z.Z. Wang, Q. Wang, Mater. Lett. 138 (2015) 212–215.
[34] X. Zhao, L.L. Shi, J. Xu, Mater. Sci. Eng. C 33 (2013) 3627–3637.
[35] X.P. Lu, Y.Y. Chen, C.Y. Zhang, T. Zhang, B.X. Yu, H.B. Xu, F.H. Wang, J. Electrochem. Soc. 165 (2018) C601–C607.
[36] X.B. Zhang, Z.X. Ba, Z.Z. Wang, Y.J. Xue, Corros. Sci. 105 (2016) 68–77.
[37] A. Srinivasan, C. Blawert, Y. Huang, C.L. Mendis, K.U. Kainer, N. Hort, J. Magnes. Alloys 2 (2014) 245–256.
[38] K. Schlüter, Z.M. Shi, C. Zamponi, F.Y. Cao, E. Quandt, A. Atrens, Corros. Sci. 78 (2014) 43–54.
[39] N.N. Aung, W. Zhou, Corros. Sci. 52 (2010) 589–594.
[40] Z.M. Shi, A. Atrens, Corros. Sci. 53 (2011) 226–246.
[41] T. Zhang, Y.W. Shao, G.Z. Meng, Z.Y. Cui, F.H. Wang, Corros. Sci. 53 (2011) 1960–1968.
[42] T. Zhang, G.Z. Meng, Y.W. Shao, Z.Y. Cui, F.H. Wang, Corros. Sci. 53 (2011) 2934–2942.
[43] G.L. Song, A. Atrensa, M. Darguscha, Corros. Sci. 41 (1999) 249–273.
[44] G. Song, A. Atrens, D. Stjohn, J. Nairn, Y. Lit, Corros. Sci. 39 (1997) 855–875.
[45] J. Chen, J.Q. Wang, E.H. Han, J.H. Dong, W. Ke, Electrochim. Acta 52 (2007) 3299–3309.
[46] X.W. Guo, J.W. Chang, S.M. He, W.J. Ding, X. Wang, Electrochim. Acta 52 (2007) 2570–2579.